Vortex-induced instabilities and accelerated collapse due to inertial effects of density stratification

HARISH N DIXIT AND RAMA GOVINDARAJAN†

Engineering Mechanics Unit, Jawaharlal Nehru Centre for Advanced Scientific Research,
Bangalore 560064, India

A vortex placed at a density interface winds it into an ever-tighter spiral. We show that this results in a combination of a centrifugal Rayleigh–Taylor (CRT) instability and a spiral Kelvin–Helmholtz (SKH) type of instability. The SKH instability arises because the density interface is not exactly circular, and dominates at large times. Our analytical study of an inviscid idealized problem illustrates the origin and nature of the instabilities. In particular, the SKH is shown to grow slightly faster than exponentially. The predicted form lends itself for checking by a large computation. From a viscous stability analysis using a finite-cored vortex, it is found that the dominant azimuthal wavenumber is smaller for lower Reynolds number. At higher Reynolds numbers, disturbances subject to the combined CRT and SKH instabilities grow rapidly, on the inertial time scale, while the flow stabilizes at low Reynolds numbers. Our direct numerical simulations are in good agreement with these studies in the initial stages, after which nonlinearities take over. At Atwood numbers of 0.1 or more, and a Reynolds number of 6000 or greater, both stability analysis and simulations show a rapid destabilization. The result is an erosion of the core, and breakdown into a turbulence-like state. In studies at low Atwood numbers, the effect of density on the inertial terms is often ignored, and the density field behaves like a passive scalar in the absence of gravity. The present study shows that such treatment is unjustified in the vicinity of a vortex, even for small changes in density when the density stratification is across a thin layer. The study would have relevance to any high-Péclet-number flow where a vortex is in the vicinity of a density-stratified interface.

1. Introduction

Vortical structures are subject to instabilities of various kinds, a common cause for the instability being the existence of other vortical structures in the neighbourhood. The Crow instability (Crow 1970) for a counter-rotating vortex pair of small core is well known. Vortices of finite core, rendered non-axisymmetric (often elliptic) by the strain field of their neighbours, are then unstable to shorter wavelength disturbances (see e.g. Kerswell 2002). Miyazaki & Fukumoto (1992) and Itano (2004) studied the effect of stratification of density perpendicular to the vortex axis on these elliptical instabilities. Both found that stratification suppresses the elliptical

† Email address for correspondence: rama@jncasr.ac.in

instability. When placed in a density-stratified fluid with the stratification parallel to their axes, systems of two or more vortices display the zigzag instability (Billant & Chomaz 2000). An important effect of density stratification, acting through such instabilities or otherwise, is to flatten out the structures and make the flow quasi two-dimensional. This property, and the variety of applications, has made the dynamics of vortical structures in a density-stratified environment a subject of much interest. The instabilities mentioned above are all three-dimensional, and involve more than one vortex. Under the Boussinesq approximation, a perpendicular density stratification has been studied in two dimensions by Brandt & Nomura (2007) in the context of vortex merger. It is shown that at a Prandtl number of 1 and Reynolds numbers above 2500, a stable density stratification aids vortex merger by speeding up their approach towards each other.

The present study is of a lone vortex with its axis perpendicular to the plane of density stratification, with no gravity. For this geometry the dominant effects are again expected to be of two-dimensional nature. An initially flat density interface is wound up into an increasingly tightened spiral by the vortex, similar to how it would advect a patch of passive scalar (see e.g. Moffatt & Kamkar 1983; Flohr & Vassilicos 1997). It is shown that two kinds of instabilities, of a Rayleigh–Taylor (RT) and Kelvin–Helmholtz (KH) types are then triggered. The former arises from a mechanism similar to the centrifugal-acceleration driven RT instability of a vortex with a heavy core, as studied by Greenspan (1968), Saunders (1973), Fung & Kurzweg (1975), Fung (1983), Sipp *et al.* (2005) and Joly, Fontane & Chassaing (2005). The latter arises purely from the fact that the density interface, being spiral, is not quite circular. Both instabilities would be missed upon neglecting inertial effects due to density variations, i.e. we need to include non-Boussinesq effects. Gravity is unnecessary in this process, and if it existed, would only act to aid the instability in some regions and slow it down in others. Here, and in the following, by the term 'non-Boussinesq', we mean the inclusion of density stratification effects in inertial terms. Note that for simplicity we neglect variations in the transport coefficients.

A work of relevance that must be discussed here is that of a stratified mixing layer of Reinaud, Joly & Chassaing (2000). By an inviscid simulation, it is shown that this flow disintegrates into turbulence. The process begins with the creation of vorticity braids by the traditional KH mechanism. Subsequently, baroclinic torque enhances the vorticity in portions of the braid and decreases it in others. The vorticity-enhanced regions are further susceptible to a secondary instability, which speeds up the disintegration of the mixing layer. An extension of this study to three-dimensional viscous situations by Fontane & Joly (2008) showed an increase in the growth of the instability. Importantly the mechanism of vorticity enhancement, due to centrifugal forces, is similar to that of the vorticity creation we shall see in the spiral interfaces below. The present work however addresses a different flow situation, of density interfaces in the vicinity of vortices. We show that the density interfaces that initially respond passively to the vortex, can ultimately be the cause for the destruction of the main vortex itself. The simplicity of the model configuration allows the analytical treatment of §2, showing the density interfaces to form Lituus spirals, where the baroclinic vorticity may be estimated as a function of distance from the central vortex core, and time. The instability of the model basic flow is studied, and the effect of various parameters, including viscosity, evaluated. We show that sharp density interfaces can lead to non-Boussinesq effects even at low Atwood numbers. It is also seen that the net effect of alternately placed stabilizing and destabilizing density jumps is one of rapid destabilization.
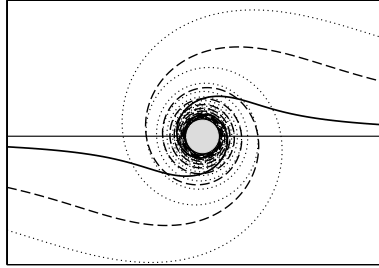
FIGURE 1. Evolution with time of an initially horizontal density interface due to a point vortex at the origin. The dotted line is at a later time than the dashed line, which in turn has evolved from the solid line. At finite Péclet number, the density would be homogeneous within a radius of $r_h \sim Pe^{1/3}(\kappa t)^{1/2}$, indicated by the grey circle.

We begin in §2.1 with the simplest model, of a point vortex at a sharp density interface. The flow is taken to be inviscid with zero-density diffusion. We discuss the formation and evolution of the spiral, and a scale for the density homogenized region close to the core. For studying the instabilities, the density jumps are first modelled as circular, and then in §2.2 as spirals. With the replacement of a point vortex by a Rankine vortex (§2.3), conditional stabilization is obtained at the edge of the vortex core, while in the interior, the growth rate is constant. In the above, analytical solutions were obtained using step changes in density and vorticity. In §3, the effect of viscosity, and of smooth vorticity and density profiles are considered. The eigenvalue problem is solved using Chebyshev collocation, and the dominant azimuthal wavenumber and growth rates are obtained for various conditions. Section 4 consists of direct numerical simulations, of inviscid flow, and of viscous flow at finite diffusivity, by a spectral method. The inviscid simulations include a small hyperviscosity and hyperdiffusivity which cutoff numerical (and other) contributions to high wavenumbers. Linear effects are displayed up to some time, with good qualitative agreement with the predictions of §§2 and 3. Afterwards vortex roll-up and other nonlinear effects are seen, including the appearance of a turbulence-like state at later times.

The predictions made here have relevance whenever a vortex and a relatively sudden density change coexist in the same neighbourhood. A cyclone close to a coastline, moving towards it with a velocity component parallel to it, could be one such situation. The actual contribution of the present instability in weakening the cyclone are unclear, since a cyclone is a complicated entity with barriers which protect it from annihilation, but it would be revealing to examine this problem using the non-Boussinesq equations. Other situations where this mechanism could apply would be in modifying submarine signatures or in an aircraft trailing vortex descending in a stratified atmosphere.

2. Inviscid stability analysis

2.1. *A point vortex and a sharp density interface*

Consider a point vortex of circulation Γ located at an initially straight density interface, with a jump $\Delta\rho$ in density across it. The flow is taken to be inviscid, and with zero diffusivity ($\kappa = 0$) of the density field. The initial interface is represented as a horizontal line in figure 1 but, since we do not take gravity into consideration, its orientation does not matter. The point vortex causes a spiralling of the density interface, whose evolution is shown in the same figure. Note that each point on the
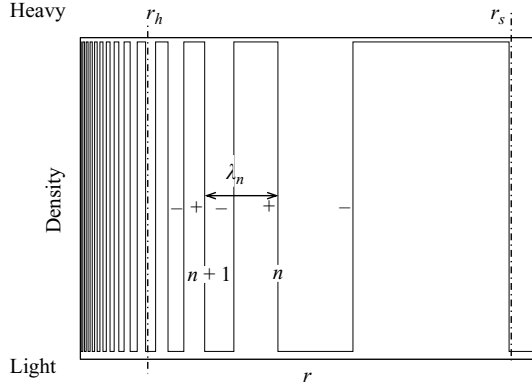
FIGURE 2. An instantaneous radial cross-section of the density profile showing the r^3 scaling of the spacing λ between neighbouring density jumps. If the diffusivity were to be finite, the density would be homogenized to its average value at radial distances below r_h. Both the homogenized front and the location r_s of the largest spiral move radially outward with time as $t^{1/2}$. For large Pe, $r_s \gg r_h$.

interface moves in a circular path at an azimuthal velocity $U = \Gamma/(2\pi r)$, where r is its radial distance from the vortex. In the initial phase of the dynamics, the interface advects passively, until its configuration allows instabilities to set in. This will be confirmed in the numerical simulations of the full equations in §4.

At a given time t, let r_n be the radial location where the interface has completed n full rotations as shown in figure 2. Then $n = \Gamma t/4\pi^2 r_n^2$, and the spacing λ_n between two zero crossings for density jumps of same sign is given by

$$\lambda_n = r_n - r_{n+1} = \sqrt{\frac{\Gamma t}{4\pi^2 n}} - \sqrt{\frac{\Gamma t}{4\pi^2 (n+1)}}. \tag{2.1}$$

To obtain the spacing between jumps of opposite sign, $n+1$ must be replaced by $(n+1/2)$ in the above formula. For large n, the spacing between successive turns of the spiral thus scales as

$$\lambda_n \sim \frac{r^3}{\Gamma t}. \tag{2.2}$$

Figure 2 shows an instantaneous density profile at time t in a radial cross-section across the spiral structure. The density jumps alternately to the values ρ_l and $\rho_h = \rho_l + \Delta\rho$ of the light and heavy fluid, respectively. In accordance with (2.2), the spacing between successive jumps rapidly increases away from the origin with an r^3 scaling. If for a moment we take the diffusivity κ to be small but non-zero, corresponding to a finite Péclet number $Pe \equiv \Gamma/\kappa$ and a diffusion length scale $l_d \sim (\kappa t)^{1/2}$, we see that for $\lambda_n < l_d$, diffusion would have erased the jumps, and homogenized the density to its average value $\rho_{ave} = (\rho_l + \rho_h)/2$. The radius r_h of this homogenized front would scale, given (2.2), as

$$\frac{r_h}{l_d} \sim Pe^{1/3}, \tag{2.3}$$

while inertia would dictate that the spiral extend up to a radial distance

$$r_s \sim l_d Pe^{1/2}. \tag{2.4}$$

The instantaneous size r_s of the spiral may be taken, for example, to be equal to the location where the interface has completed one rotation. For a Péclet number tending to infinity, we expect many density jumps to exist between r_h and r_s. By different and more general approaches, Moffatt & Kamkar (1983), Rhines & Young (1983), Flohr & Vassilicos (1997) and Bajer, Bassom & Gilbert (2001) had obtained scaling equivalent to (2.3) for the accelerated diffusion of passive scalars near a vortex, due to the accumulation of discontinuities. Incidentally, Gilbert (1988) showed how spiral structures forming around coherent vortices affect the spectrum of two-dimensional turbulence.

We now study the linear stability of an instantaneous snapshot of the flow, taking the base flow to be slowly varying in time. The assumption is akin to the parallel flow approximation in space for spatially developing flows such as in boundary layers, and is valid when the change in the structure is much slower than the frequency of the dominant disturbance, which we shall see to be the case for disturbances of high azimuthal wavenumber. We first appproximate the spiral density interface by concentric circles of radii r_j, $j = 1, 2, 3, \ldots n$ which are spaced as $r_j - r_{j-1} \sim r_j^3$. The fact that the spiral is different from a series of circles is also important, and instructive to study separately. This is done in § 2.2. Here n step changes in density are under consideration, and the density (for $r > r_h$) is given by

$$\bar{\rho} = \rho_{ave} \pm \frac{(-1)^j}{2} \Delta \rho, \qquad r_{j-1} < r < r_j. \tag{2.5}$$

The density of the innermost layer, just beyond r_h, hops between ρ_l and ρ_h with time, and subsequent jumps alternate in sign. The vorticity and density balance equations are given in the inviscid, infinite Péclet number limit by

$$\bar{\rho} \frac{\mathrm{D}\Omega}{\mathrm{D}t} = -\nabla \bar{\rho} \times \frac{\mathrm{D}\boldsymbol{u}}{\mathrm{D}t}, \tag{2.6}$$

$$\frac{\mathrm{D}\bar{\rho}}{\mathrm{D}t} = 0, \tag{2.7}$$

where $\mathrm{D}/\mathrm{D}t \equiv \partial/\partial t + \boldsymbol{u} \cdot \nabla$, and $\boldsymbol{u} = (u_r \boldsymbol{e}_r, u_\theta \boldsymbol{e}_\theta)$, Ω and ρ denote the velocity vector (of radial and azimuthal components), the vorticity and the density respectively. The flow is taken to be incompressible, so $\nabla \cdot \boldsymbol{u} = 0$. If the density in (2.6) were to be replaced by its average value, that would constitute a neglect of non-Boussinesq effects. The right-hand side would then be zero, and the flow would remain irrotational forever except at the origin. For small Atwood number

$$\mathscr{A} \equiv \frac{\Delta \rho}{\rho_h + \rho_l}, \tag{2.8}$$

this approximation is made most often, but we shall see that not making this approximation is crucial to obtaining the correct, and dramatic, dynamics of this flow.

Linearizing (2.6) about the base flow, assuming the perturbations to be of normal mode form, e.g. $\hat{u}_r = u_r(r) \exp[\mathrm{i}(m\theta - \omega t)]$, and eliminating u_θ, we get

$$\left\{ \frac{r^2 \bar{\rho}}{m^2} \left(\omega - \frac{mU}{r} \right) \left(u_r' + \frac{u_r}{r} \right) + \frac{r\bar{\rho}}{m} \left(U' + \frac{U}{r} \right) u_r \right\}' - \bar{\rho} \left(\omega - \frac{mU}{r} \right) u_r$$

$$- \bar{\rho} \frac{2U}{m} \left(u_r' + \frac{u_r}{r} \right) = \frac{-U^2 \bar{\rho}'}{r(\omega - mU/r)} u_r. \tag{2.9}$$

Around a point vortex, the mean azimuthal velocity $U = \Gamma/(2\pi r)$, and the primes denote differentiation with respect to the radial coordinate r. The step changes in density shown in (2.5) correspond to delta functions in its derivative, $\rho' \equiv (-1)^{j+1} \Delta\bar{\rho}\,\delta(r - r_j)$. Away from the discontinuities, (2.9) may be simplified to

$$\mathscr{I}u_r \equiv \left(\omega - \frac{mU}{r}\right)\left[r^2 u_r'' + 3r u_r' - (m^2 - 1)u_r\right] + mr\,\Omega' u_r = 0. \qquad (2.10)$$

For a point vortex, the gradient of the vorticity $\Omega' = 0$ for $r > 0$ (but Ω' assumes non-zero values in §2.3). The solutions are of the form

$$u_r = P_j r^{m-1} + Q_j r^{-m-1}, \qquad j = 0, 1, \ldots n. \qquad (2.11)$$

Since u_r is a linear eigenfunction, one of the constants P_j, Q_j may be fixed arbitrarily. The remaining $2n + 1$ constants and the unknown eigenvalue ω may be resolved as follows. The perturbed density interfaces are located at $r = (r_j + \hat{\eta}_j)$, $j = 1, 2, 3, \ldots n$. Integrating (2.9) between $\eta_j - \epsilon$ and $\eta_j + \epsilon$ for $\epsilon \to 0$ we get n jump conditions

$$\Delta_\eta \left\{ \frac{r^2 \bar{\rho}}{m^2}\left(\omega - \frac{mU}{r}\right)\left(u_r' + \frac{u_r}{r}\right) + \frac{r\bar{\rho}}{m}\left(U' + \frac{U}{r}\right)u_r \right\} = \left(\frac{-U^2 u_r}{r(\omega - mU/r)}\right)_\eta \Delta_\eta(\bar{\rho}), \qquad (2.12)$$

where

$$\Delta_\eta\{f\} = f|_{r_j + \eta_j + 0} - f|_{r_j + \eta_j - 0}. \qquad (2.13)$$

Recognizing that u_r is continuous at each interface, and decays to zero both at $r = 0$ and as $r \to \infty$, gives $n + 2$ more conditions. The system may then be simplified into a dispersion relation for ω in the form of a polynomial of degree $2n$.

For a single circular density jump at $r = r_1$ the dispersion relation is

$$\omega = \frac{m\Gamma}{r_1^2} \pm \sqrt{-\frac{m\Gamma^2}{r_1^4}\frac{(\rho_0 - \rho_1)}{(\rho_0 + \rho_1)}}, \qquad (2.14)$$

and the frequency and growth rate of the perturbation are given respectively by the real and imaginary parts of ω. The flow is unstable to perturbations of any azimuthal wavenumber when $\rho_0 > \rho_1$, i.e. when there is heavy fluid inside and light fluid surrounding it. This result is perfectly analogous to a planar RT instability (see e.g. Drazin & Reid 1981), with gravity replaced by the centrifugal acceleration at a given radius. We shall return to this in §2.3. It may also be derived from Rayleigh's criterion for centrifugal instability, modified to account for density. In this context, von Kármán (see Lin 1955) proposed that $d(\bar{\rho}U^2 r^2)/dr \geqslant 0$ for stability. Yih (1961) showed that the above criterion is neither necessary nor sufficient, and that $d\bar{\rho}/dr \geqslant 0$ and $d(U^2 r^2)/dr \geqslant 0$ are required separately, for stability. Other stability criteria have been formulated, notably by Howard & Gupta (1962) and Leibovich (1969) for axisymmetric and non-axisymmetric disturbances. A comprehensive review is given in Sipp *et al.* (2005). Fung & Kurzweg (1975) and Fung (1983) wrote down expressions similar to ours above for simple artificially prescribed circular RT+KH situations.

In the present flow, $4\pi^2 U^2 r^2 = \Gamma^2$ is constant for $r > 0$, while Yih's first criterion (Yih 1961) is violated when light fluid surrounds heavy. The perturbation eigenfunction describes a circular vortex sheet at r_1 of strength

$$\Delta u_\theta = -2i u_r,$$

which is independent of the density difference. When the density difference $\Delta\rho$ goes to zero, the system would support a neutral mode with the above eigenfunction, one
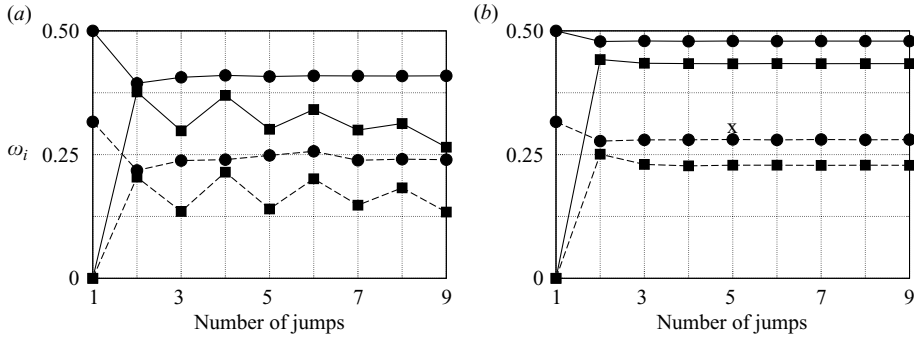
FIGURE 3. Maximum growth rate of disturbance as a function of the number of density jumps. The solid lines correspond to $m = 5$ and the dashed lines to $m = 2$. The circles show the growth rate with the innermost fluid layer being heavy, at $\rho_h = 1.05$, while squares are for this layer being light, at $\rho_l = 0.95$. The first two jumps are located at (*a*) $r_1 = 0.1, r_2 = 0.102$ (*b*) $r_1 = 0.1, r_2 = 0.105$, with the remaining jumps spaced out as r^3. The growth rate has been normalized by Γ/r_1^2.

among the continuous spectrum of non-Kelvin modes (A. Roy & G. Subramanian, personal communication). Just as a disturbance of small wavelength in a boundary layer does not perceive the downstream growth of the boundary layer, a disturbance of large azimuthal wavenumber riding on the interface at a certain radial location does not perceive the time variation in the spiral structure of the interface. At low wavenumbers too, our results shown in figure 3 indicate that the growth rate of the instability is insensitive to the spacing between the jumps, so a frozen interface approximation appears to be valid here too. However, for completeness, a global instability analysis accounting for the time variation of the spiral would be warranted.

   Figure 3 shows the growth rate ω_i of the instability with multiple density jumps of size $\Delta\rho = \pm 0.1$, obtained using Mathematica. The single jump ($n = 1$) result is as in (2.14). In the two jump case, the second jump, being of opposite sign, partially neutralizes the first. When the initial jumps are very closely spaced, the growth rate oscillates with the addition of jumps as shown in figure (3*a*), but when they are not too close (figure 3*b*), the growth rate after the first few jumps is insensitive to further addition of either a stabilizing or a destabilizing jump. Note that the growth rate of the instability is substantial, of the same order of magnitude as the inverse of the inertial time scale, whether the first jump is positive or negative. In other words, the flow is quite unstable irrespective of whether the central region is light or heavy. This result is different from the requirement of a heavy core in earlier work on a single stratified layer (Joly *et al.* 2005; Sipp *et al.* 2005). The eigenfunctions in the radial and azimuthal direction corresponding to five jumps with a heavy inner layer are shown in figure 4, the behaviour is as expected.

2.2. *Deviation of a spiral density interface from a circular interface*

We have so far assumed the density interface to be in the form of several concentric circles, while it actually is two continuous spirals originating from the flat interface on either side of the vortex. At a given time t, the spiral interface created by a point vortex is described in cylindrical polar coordinates by
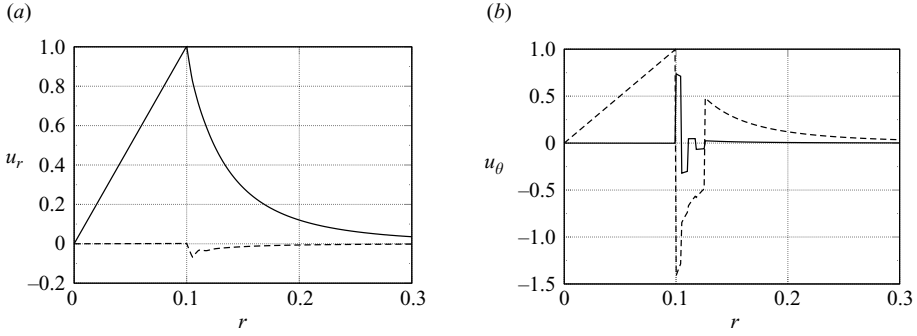
$$\theta_s = \frac{\Gamma t}{2\pi r^2}. \tag{2.15}$$

FIGURE 4. (*a*) Radial and (*b*) azimuthal eigenfunctions for a point vortex with 5 density jumps placed with an r^3 spacing, corresponding to the point marked **X** in figure 3(*b*). The solid and dashed lines show the real and imaginary parts, respectively.
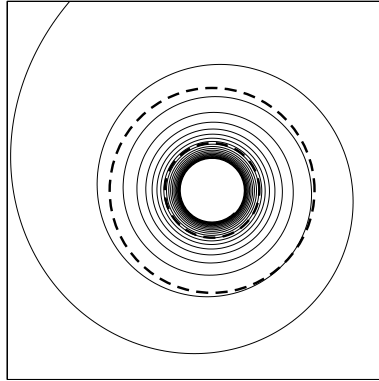

FIGURE 5. A Lituus spiral describing the instantaneous shape of one side of the density interface. The dashed lines describe circles. It is seen that the assumption of a circular jump made hitherto is better at smaller radii, or at later times at a given radius.

The instantaneous interface is thus a pair of Lituus spirals (one among the Archimedean class of spirals), one of which is shown in figure 5. From (2.15) we may obtain the angle α between the spiral and a circle sharing the same origin and radius as

$$\tan \alpha = \frac{\pi r^2}{\Gamma t}, \tag{2.16}$$

so the assumption of a circular interface is better at smaller radii or late times.

Returning to the vorticity (2.6) and assuming that the effect of the circulation Γ of the point vortex is far greater on the basic flow than of that which is newly created, we may write

$$\frac{\mathrm{D}\Omega}{\mathrm{D}t} \simeq -\frac{\nabla\bar{\rho}}{\bar{\rho}} \times \left[\frac{U^2}{r} \boldsymbol{e}_r \right]. \tag{2.17}$$

Under this approximation, the streamlines remain circular. In §4 this approximation is shown to be valid even up to the nonlinear regime at later times (figure 18*a*). We see that vorticity is created whenever the gradient of the density is not strictly radial, i.e. for any deviation from a circular interface. Note that this too is a non-Boussinesq effect. Since $\nabla\bar{\rho} = \pm \Delta\rho\delta(r\theta - r\theta_s)\boldsymbol{n}$, where $\boldsymbol{n}$ is a unit vector in the direction normal

j	$\Delta\rho$	$(\Delta U_\theta)_j$	ω_i (CRT alone)	ω_i (CRT + SKH)
1	0.1	-0.805	0.5	0.6469
2	-0.1	0.720	0.4783	0.5364
3	0.1	-0.634	0.4795	0.5568
4	-0.1	0.547	0.4789	0.5407

TABLE 1. Rates of instability growth for a purely centrifugal RT instability and a combined CRT and SKH instability with multiple jumps. Larger growth rates are obtained for the combined instability. The number of jumps is denoted by j. The size of the density jump $\Delta\rho$ and that of the last velocity jump $(\Delta U_\theta)_j$ across the interface are fixed arbitrarily. At later times or lower radius, ΔU_θ would be much higher, so the SKH can give rise to extremely large disturbance growth rates. Here $r_1 = 0.1$, $r_2 = 0.105$ and $m = 5$. Column 4 corresponds to the uppermost curve in figure 3(b).

to the spiral, using (2.16) we may write

$$\frac{\mathrm{D}\Omega}{\mathrm{D}t} \simeq \frac{\pm\Delta\rho}{\rho_{ave}} \frac{U^2}{r} \frac{1}{(1 + 4\theta_s^2)^{1/2}} \delta(r\theta - r\theta_s). \tag{2.18}$$

The above equation may be integrated in time at a given r, i.e. moving with the interface on its circular path, to give

$$\Omega(r, t) = \mp \mathscr{A} U \log\left(2\theta_s + \left(1 + 4\theta_s^2\right)^{1/2}\right)\delta(r\theta - r\theta_s) \equiv \Delta U_\theta \delta(r\theta - r\theta_s). \tag{2.19}$$

At high θ_s, i.e. at large time at a given radius, we have

$$\Delta U_\theta \simeq \mp \mathscr{A} U \log\left(\frac{2\Gamma t}{\pi r^2}\right). \tag{2.20}$$

At every unstable density jump, negative vorticity is created and vice versa, resulting in heavier fluid travelling faster and lighter fluid slower. A spiral Kelvin–Helmholtz (SKH) instability thus ensues, and combines with the centrifugal Rayleigh–Taylor (CRT) instability. We shall see in figure 18(b), §4 that such jumps in the azimuthal velocity are obtained in the full numerical solution as well. For a single jump, approximating it to be circular for the purpose of studying the instability, we now have the dispersion relation

$$\omega = \frac{m}{r_1(\rho_0 + \rho_1)}\left[\rho_0 U_0 + \rho_1 U_1 \pm \sqrt{\frac{(\rho_1 U_1^2 - \rho_0 U_0^2)(\rho_0 + \rho_1)}{m} - \rho_0\rho_1(U_0 - U_1)^2}\right], \tag{2.21}$$

where $U_0 = U$ and $U_1 = U + \Delta U_\theta$. The first term under the square root sign would reduce to a radial gravity term if we set the velocity difference to zero. The second term under the square root sign is responsible for the SKH instability. At short times, ΔU_θ is small, so the instability reduces to the Rayleigh–Taylor one of (2.14). At large times or at low Atwood number, instability growth would be dictated by the velocity jump ΔU_θ. Given that ΔU_θ increases logarithmically in time, we have a spiral KH instability with a slightly faster than exponential growth rate, i.e. $u_r \sim t^t$.

Table 1 compares disturbance growth rates between a purely CRT instability and a combined CRT and SKH instability. Depending on the time chosen, the growth rates for the combined instability can become extremely large. In any case, the combined instability has a larger growth rate than the CRT alone. Note that the interface is unstable everywhere, irrespective of the local sign of the density jump.
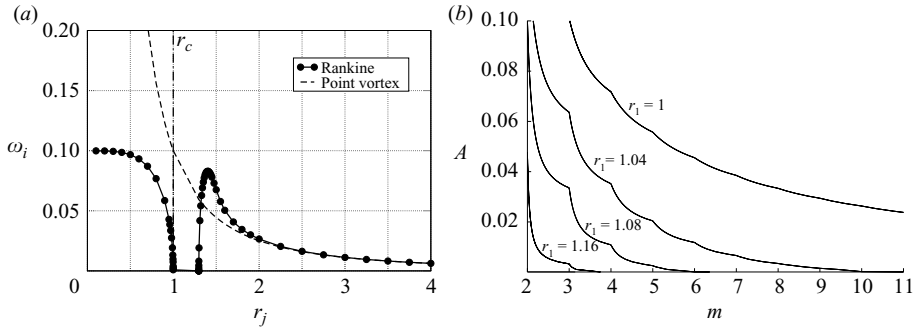
FIGURE 6. (*a*) Comparison of the growth rates due to a Rankine vortex with $r_c = 1$ and a point vortex for $\mathscr{A} = 0.005$ with $m = 2$ and (*b*) stability domain in the $\mathscr{A} - m$ plane for various jump locations. The region above each curve is unstable, and solid lines between integer values of m are only to guide the eye.

In the work of Reinaud *et al.* (2000), the flow is of mixing layer type, and therefore already unstable. Baroclinic torque in that case serves to increase the vorticity in one part of the mixing layer allowing a secondary instability to set in, thus contributing to a speeding up of the breakup process. In contrast, the SKH is a primary instability, with the vortex sheets entirely generated by baroclinic torque. In combination, the SKH and CRT instabilities rapidly destabilize a flow which would otherwise survive for an extremely long time.

2.3. *Rankine vortex*

The point vortex is replaced by a Rankine vortex, with a core of radius r_c and constant vorticity Ω_0. The vorticity outside is zero. As will be seen in the numerical simulations in §4, the exact form of the vorticity does not affect the results much so long as it is concentrated within a small core. The approach for obtaining disturbance growth rates is as before, except that we obtain a polynomial equation for ω which is one order higher, e.g. a cubic for a single jump in the place of the quadratic (defined in (2.14)).

As expected, a jump far away from the core responds exactly as to a point vortex, so the primary effect of a finite core is in the case where a jump is placed in the vicinity of the core. As can be seen in figure 6(*a*) the instability growth rate is constant and has a large value when the density jump is placed inside the core. This could ultimately lead to the destruction of the core. Configurations similar to the one in this subsection, i.e. instabilities due to heavy-cored vortices, were studied by Sipp *et al.* (2005) and Joly *et al.* (2005). In both, Gaussian vorticity and density profiles were used instead of the discontinuous profiles used here. Due to this, quantitative comparisons with their results cannot be made. Qualitatively, in their case too, instability with large growth rate was found. For density jumps inside the core, growth rate saturates at a large value as the location of the density jump approaches the origin. A similar feature was observed by Joly *et al.* (2005) (see their figure 6*a*) when the density core was made very small.

When the density jump is placed close to the edge of the core, figure 6(*a*) shows that the instability vanishes suddenly. This result is in qualitative agreement with Sipp *et al.* (2005), who found stabilization when the density-stratified layer overlapped with the region of high shear. A similar observation was made indirectly by Joly *et al.* (2005). This stabilization may be seen explicitly in the simplest case when the density

jump is exactly placed at the edge of the Rankine core. There the growth rate is described by a quadratic rather than a cubic equation in ω, and written as

$$\omega = m\Omega_0 - \left[\frac{\Omega_0}{1+s}(1 \pm \sqrt{1-m(1-s^2)}) \right], \qquad (2.22)$$

where $s = \rho_l/\rho_h$. This puts a condition $m > 1/(1-s^2)$ for instability. The cubic equation in ω, when the two discontinuities are near each other but do not coincide, gives solutions consistent with this condition. From these solutions, we may say a little more about the neutral region seen in figure 6(*a*). As $\Delta\rho \to 0$, we recover the neutral Kelvin mode, and a mode with $\omega = mU/r$ in the continuous spectrum. When $\Delta\rho \neq 0$, apart from this Kelvin mode with modified frequency, two neutral waves are supported, which travel in a direction opposite to the previous continuous-spectrum mode. These additional waves are analogous to internal gravity waves in a planar problem with gravity. On either increasing $\mathscr{A}$ or m, these waves destabilize. Density variations within the vortex core and near the edge often give rise to interesting features, such as a destabilization of a lighter core in some cases. These are being studied, and are not discussed further here to avoid diversion from our present focus.

In this idealized model, the instability grows indefinitely for any $\mathscr{A}$ as $\omega_i \sim \sqrt{m}$. In reality, at high Péclet number, a mode with azimuthal wavelength comparable to the thickness of the density-stratified layer will grow faster than the others, similar to what would happen in a planar situation (Drazin & Reid 1981). Diffusivity and viscosity would further affect the results, as shown in the next section.

3. Viscous stability analysis

Rather than a parametric study, which is very tedious given the number of parameters involved in the viscous problem, the purpose of this section is to present characteristic results, some of which will serve for comparison with the numerical simulations of §4. We restrict ourselves to Atwood numbers between 0.05 and 0.2, and the relevant Reynolds numbers are 2000 and above. We present results for (i) the effects of viscosity on the CRT instability with one and two density jumps, and (ii) the effect of viscosity, interface thickness, and Atwood number separately on the combined CRT and SKH instability for two jumps. This is deemed sufficient since it has been demonstrated in §2 that the result for multiple jumps is well approximated by that for two jumps in either order. We again assume that the density interface is circular, and introduce vortex sheets at the density interface as described. The edge of the Rankine vortex, and the density profile within each density interface are made smooth by specifying $\Omega/\Omega_0 = (1-\tanh((r-r_c)/d))/2$ and $\bar{\rho}/\rho_a = 1 \pm \mathscr{A} \tanh((r-r_j)/d)$ in the neighbourhood. For simplicity the smoothing parameter d is kept the same for vorticity and for each density interface. The equations are non-dimensionlized by the vortex core size r_c as the characteristic length scale, and the velocity at the edge of the core U_c as the characteristic velocity scale. The Reynolds number is defined as $Re \equiv \Gamma/\nu$, the Péclet number as $Pe \equiv \Gamma/\kappa$ where ν and κ are the kinematic viscosity and scalar diffusivity respectively, and the circulation $\Gamma = 2\pi U_c r_c$. The Atwood number is defined as $\mathscr{A} \equiv \Delta\rho/(\rho_h + \rho_l)$. The densities are scaled by the average density $\rho_a = (\rho_h + \rho_l)/2$, ρ_h and ρ_l being the heavy and light densities respectively. In this study the Schmidt number $Sc = \nu/\kappa$ is held constant at 10. Higher values of Sc are expected to show similar behaviour. The stability equations in the

non-dimensional form may now be written as

$$\bar{\rho}r^2\mathscr{I}u_r + \bar{\rho}'r^3\left[\left(\omega - \frac{mU}{r}\right)\left(r\frac{\mathrm{d}}{\mathrm{d}r} + 1\right) + m\Omega\right]u_r + \mathrm{i}m^2rU^2\rho = \frac{\mathrm{i}}{Re}\mathscr{N}u_r, \quad (3.1)$$

$$\left(\omega - \frac{mU}{r}\right)r^2\rho = -\mathrm{i}u_r r^2\bar{\rho}' + \frac{\mathrm{i}}{Pe}\mathscr{M}\rho, \quad (3.2)$$

where the operator $\mathscr{I}$ is as defined in (2.10), and

$$\mathscr{N} \equiv r^4\frac{\mathrm{d}^4}{\mathrm{d}r^4} + 6r^3\frac{\mathrm{d}^3}{\mathrm{d}r^3} + (5 - 2m^2)r^2\frac{\mathrm{d}^2}{\mathrm{d}r^2} - (1 + 2m^2)r\frac{\mathrm{d}}{\mathrm{d}r} + (m^2 - 1)^2, \quad (3.3)$$

$$\mathscr{M} \equiv \left(r^2\frac{\mathrm{d}^2}{\mathrm{d}r^2} + r\frac{\mathrm{d}}{\mathrm{d}r} - m^2\right). \quad (3.4)$$

The boundary conditions are $u_r = u'_r = 0$ at $r = 0$ and $r \to \infty$, as valid for $m \geqslant 2$. Note that since we are restricted to two dimensions, the $m = 0$ mode is unphysical, and $m = 1$ is only a translational mode causing no change in the structure of the vortex. Equations (3.1–3.4) are solved as an eigenvalue problem by a Chebyshev collocation method, with a grid stretching in the density-stratified layer as used in a different context in Khorrami, Malik & Ash (1989). A typical computational domain size was $25r_c$ and good accuracy was obtained with 800 collocation points. The stability calculations were validated by repeating some of the cases of Joly *et al.* (2005), and very good agreement was obtained.

In instabilities of this kind, the azimuthal wavenumber m_{max} at which the growth rate is maximum is usually the most noticeable feature even after the flow becomes nonlinear (Saunders 1973; Coquart, Sipp & Jacquin 2005; Joly *et al.* 2005). We therefore devote some attention to this parameter, and first examine how it varies with Reynolds (or equivalently, Péclet) number for a single density jump in CRT instability. In planar RT instability, increasing viscosity progressively stabilizes short wavelength perturbations, and therefore reduces the wavenumber of the 'most dangerous' mode (see Chandrasekhar 1961; Duff, Harlow & Hirt 1962). The same physics may be expected in CRT, and figure 7 shows that m_{max} increases with Reynolds number for a fixed base flow. There was no surprise in the qualitative dependence of the single jump CRT instability on the interface thickness d. The maximum growth rate (not shown) occurs for the thinnest profile, and with an increase in d the instability saturated at a smaller wavenumber, roughly as $d^2 \sim 1/m$, the reason for this scaling is unclear at his point.

We now examine the effect of introducing a second density jump, with the inner jump destabilizing and the outer one stabilizing. The thickness of the jumps is fixed at $d = 0.02r_c$. Figure 8 shows the frequency and growth rate of the CRT instability as functions of m and Re. The highest Reynolds number shown is close to the inviscid result (not shown). The growth rate, the m_{max} and the range of unstable modes all increase as the Reynolds number increases, as is to be expected. The frequency on the other hand remains similar to the inviscid predictions, showing a very weak dependence on Reynolds number.

So far, only the effects of density have been considered. We now allow both CRT and SKH instabilities to operate in combination. As a suitable base state, we chose the flow field at a non-dimensional time, which is 30 for the results presented. Choosing the location of the first jump then dictates that of the second, using (2.1) and noting that $(n + 1/2)$ should be used in place of $(n + 1)$, since the second jump, belongs to the
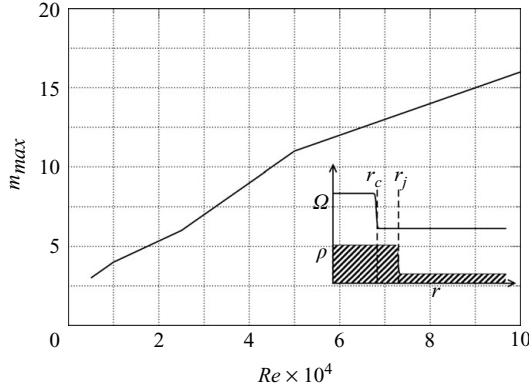
FIGURE 7. Effect of Reynolds number on a single density-jump CRT instability. The azimuthal wavenumber corresponding to maximum disturbance growth rate is shown, with $d = 0.02r_c$, $r_j = 2r_c$, $\mathscr{A} = 0.05$. A schematic of the base flow profile is shown in the inset.
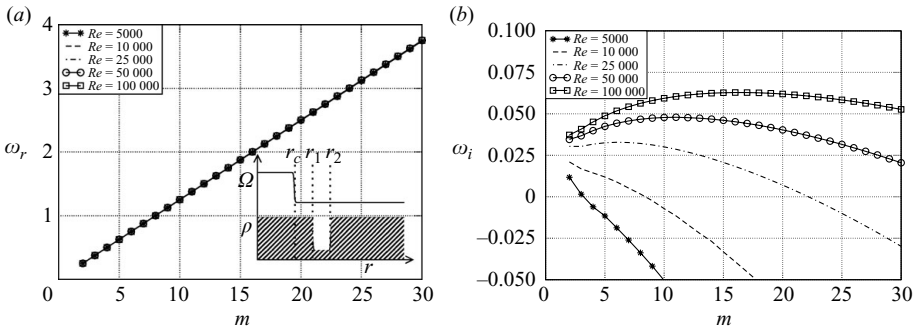

FIGURE 8. Frequency and growth rate of the most unstable CRT mode for a smooth vortex with two circular density jumps at $r_j = 2r_c$ and $r_j = 2.5r_c$. $\mathscr{A} = 0.05$, and $d = 0.02r_c$. The first jump is from heavy to light and the second jump from light to heavy. A schematic of the base flow profile is shown in the inset.

spiral sheet originating from the opposite side. The vorticity generated at the density interfaces due to the baroclinic torque is in the form of thin spiral shear layers. Since the spectral collocation method requires smooth profiles to produce reliable results, we approximate them to be circular steep Gaussians of the sign of the density jump. The idealized base flow vorticity is therefore prescribed to be

$$\frac{\Omega}{\Omega_0} = \frac{1}{2}\left(1 - \tanh\left[\frac{(r - r_c)}{d}\right]\right) \pm \sum P_j \exp\left[\frac{-(r - r_j)^2}{d^2}\right]. \tag{3.5}$$

For simplicity, the same base flow vorticity and density profiles are used to study the effects of viscosity. Though in reality, such an initial condition would relax on the viscous time-scale to a Gaussian distribution. Studying diffusive effects with jump-like profiles has been carried out in the past by Villermaux (1998), Chandrasekhar (1961) and Duff *et al.* (1962). Hence only a qualitative comparison of these viscous results can be made with experiments or DNS. Figures 10(*a*) and 10(*b*) show growth rates from inviscid and viscous stability analysis, respectively. The Atwood numbers used in the two cases are 0.2 and 0.1 respectively, which enable comparisons with simulations.
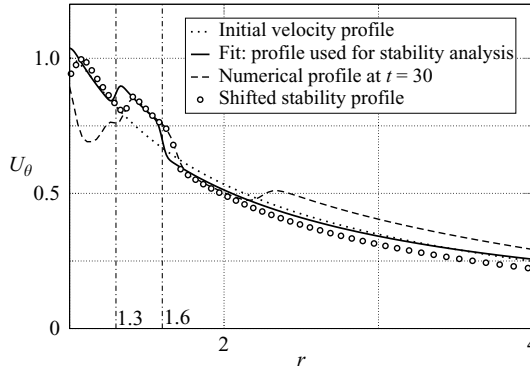
FIGURE 9. Azimuthal velocity profile outside the vortex core at $t = 30$ (in the simulations shown in figure 12). The initial velocity profile used in the numerical simulations has been shown for reference, along with the profile used in the stability analysis. A similar profile would also be obtained at t=40 (shown in figure 12).

The first jump is located at $1.3r_c$ and the location of the second is obtained to be $1.57r_c$ from (2.1), which is rounded off to $1.6r_c$. For simplicity we use $P_1 = -P_2 = 1$ in (3.5), the value chosen to roughly agree with the sheet strengths in the simulations at $t = 30$ (see §4, figure 12). The constructed stability profiles are compared with the actual numerical simulation profiles shown in figure 9. Also shown is the initial velocity profile in the simulations. To show that the jump sizes are indeed in good agreement, a slightly shifted stability profile is shown.

For the smallest thickness considered, $d = 0.01r_c$, the inviscid instability peaks at a very large value of m. For larger d, there is a non-monotonic variation of ω_i with m, which can be explained as follows. When the interfaces are thin, the dominant wavenumber is selected by their thickness, hence a large wavenumber instability is obtained. However, as the interface thickness becomes comparable to the distance between them, the fact that each interface contains a diffused vortex sheet makes the small wavenumber modes respond as to a wake-like base flow, and so the fastest growing azimuthal wavelengths are comparable to the interface spacing rather than the thickness. Very large wavenumbers again display increasing growth. A similar study with two density jumps was carried out (not shown) on the CRT instability alone, and no such behaviour was obtained in that case. The nonmonotonic variation of the growth rate with m is thus a feature of the inviscid, combined CRT and SKH instability.

The major effect of viscosity (figure 10*b*) is that the dominant wavenumbers are now much smaller, in the range of 3–5, and decreasing with Reynolds number. Also with a decrease in Reynolds number, the growth rate drops considerably. These results will be seen below to be in agreement with simulations. A critical Reynolds number R_{cr} is very difficult to define in this case since there are many parameters. An example each of stabilization due to decreasing Atwood number and increasing thickness are given by the dashed line and the filled circle in the figure, respectively. Note that the growth rates in figure 10(*b*) are lower than in figure 10(*a*) in large part because of the lower Atwood number.

The KH instability is not studied here in isolation, since it is not relevant to our flow, but we remark that planar shear layers are insensitive to viscous effects at high Reynolds numbers Villermaux (1998).
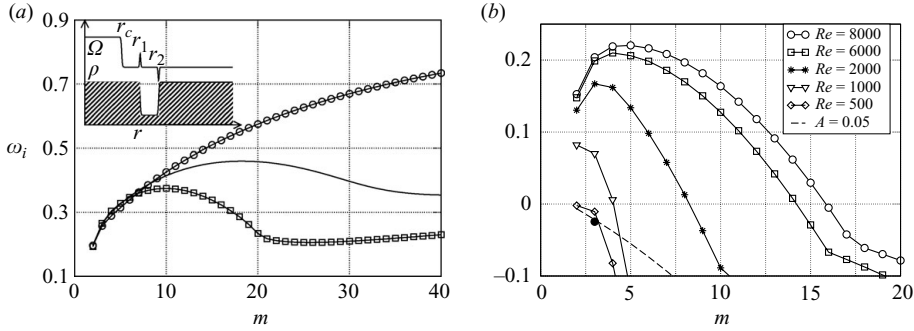
FIGURE 10. Growth rate for the combined CRT and SKH instability with a smooth vortex and two circular density and velocity jumps of same size at $r_1 = 1.3r_c$ and $r_2 = 1.6r_c$, (*a*) for varying thickness with inviscid analysis, $\mathscr{A} = 0.2$, circles: $d = 0.01r_c$, solid: $d = 0.02r_c$, squares: $d = 0.03r_c$. The base flow is shown schematically in the inset. (*b*) Viscous analysis at various Reynolds numbers for $\mathscr{A} = 0.1$, $d = 0.05r_c$. The dashed line is for $Re = 2000$ but with $\mathscr{A} = 0.05$, $d = 0.05r_c$. The lone black filled circle shows the highest growth rate for $Re = 2000$, $\mathscr{A} = 0.1$, $d = 0.2r_c$, $r_2 = 1.4r_c$.

4. Direct numerical simulations

The complete problem including non-Boussinesq effects is now solved by direct simulations. Again gravity is not considered. Both inviscid and viscous simulations are carried out, in Cartesian coordinates in a doubly periodic domain using the Fourier pseudospectral method. In all the results presented here, we use 1536 collocation points in each direction without dealiazing. No visible difference was found with dealiazing. Results did not vary significantly for grid sizes of 1024 and 2048. The computational domain is $15\pi r_c$ for the inviscid simulations and $20\pi r_c$ for the viscous simulations, which is large compared to most numerical simulations found in literature. Varying it did not alter the features of the instability. In all the figures below, x and y shown corresponds to the actual domain size scaled by a factor of π. The effects of using periodic boundary conditions for problems involving an isolated vortex is discussed in Joly *et al.* (2005) and Josserand & Rossi (2007). The residual vorticity produced because of the imposition of the periodic boundary conditions is about 800 times smaller than the vorticity of the central core at early times. With the production of baroclinic vorticity, this residual vorticity becomes 3800 times smaller than the peak value of the vorticity in the flow field. Therefore, the results of our numerical simulations can be considered to be a faithful representation of an isolated vortex.

The time discretization is done through an Adams–Bashforth scheme. We split the total density field as $\tilde{\rho} = \rho_i(y) + \rho(x, y, t)$, where ρ_i is the initial density field and ρ has information of the time evolution of the density. This allows ρ to remain a spatially periodic function, with a period equal to the domain size. As in §2.3, we non-dimensionalize the governing equations using the vortex core size, r_c as the characteristic length scale, Ω_0 as the characteristic scale for vorticity such that the circulation $\Gamma = \Omega_0 \pi r_c^2$. In Cartesian coordinates, the equations in velocity-vorticity formulation in the non-dimensional form are

$$\frac{D\Omega}{Dt} = \frac{1}{\tilde{\rho}}\left(\frac{d\rho_i}{dy} + \frac{\partial\rho}{\partial y}\right)\frac{Du}{Dt} - \frac{1}{\tilde{\rho}}\frac{d\rho}{dx}\frac{Dv}{Dt} + \frac{1}{Re}\nabla^q\Omega, \tag{4.1}$$

$$\frac{D\tilde{\rho}}{Dt} = \frac{1}{Pe}\nabla^q\tilde{\rho}, \tag{4.2}$$
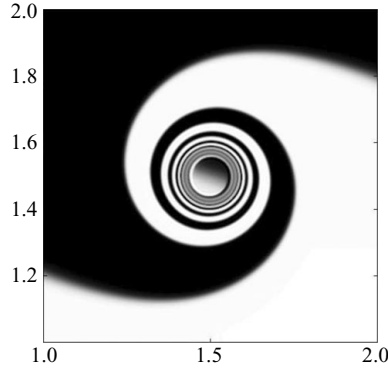
FIGURE 11. Density field forming a Lituus spiral around a Rankine vortex in an inviscid simulation treating the density field like a passive scalar. The vorticity field (not shown) is unchanged from its initial value. The black and white regions correspond to light and heavy fluid respectively. This image is formed at $t = 100$, by which time the flow will be seen to undergo a complete breakdown in the full simulations including non-Boussinesq effects. The time t is scaled by $\pi r_c^2/\Gamma$.

$$\frac{\partial u}{\partial x} + \frac{\partial v}{\partial y} = 0, \tag{4.3}$$

where q is the order of the diffusion term used, and densities are scaled by the average density. In the viscous case, $q = 2$ and $Re = \Gamma/\nu$ and $Pe = \Gamma/\kappa$ are the Reynolds and Péclet numbers, respectively. In the inviscid simulations, hyperviscous diffusion of the vorticity and density fields is included by setting $q = 6$, and Re and Pe, defined respectively in this case as $\Gamma r_c^4/\nu_h$ and $\Gamma r_c^4/\kappa_h$. The hyperviscous Re and Pe were nearly 2×10^{11}. Using twice or half of these values did not change the results qualitatively. A similar approach was used, for example, by Neilsen et al. (1996) for studying inviscid vortex merger. The purpose of the hyperviscosity is to damp out spurious numerical modes of large wavenumber, and the diffusion it causes is found to be very weak, so these simulations are referred to here as inviscid. An initial vorticity in the form of a smoothed Rankine vortex, as in §3 is used for the inviscid simulations. A Lamb–Oseen vortex with $\Omega = \Omega_0 \exp[-r^2/r_c^2]$ defines the initial vorticity in the viscous simulations. A range of Reynolds numbers from $Re = 500$–$10\,000$ were studied, and three of them are shown here as being representative. For Re larger than the range studied, the resolution was found to be insufficient at later times to capture the thin spiral structures. And for Re smaller than 2000, dissipation was too rapid for the density gradients to play any significant role. The Atwood number was also varied from 0.05 to 0.4, and it was found that lower Atwood numbers required thinner interface thickness to display the instability. At $\mathscr{A} \leqslant 0.05$ this could lead to difficulties in numerical resolution. In each case, the vortex is placed at a horizontal interface separating fluids of different densities. The interface is in the form of a thin layer within which density varies in the vertical coordinate as a hyperbolic tangent. The straight interface is in contrast to the axisymmetric initial density profile with a heavy core in the numerical simulations of Joly et al. (2005). The nonlinear terms on the right-hand side of (4.1) are computed in physical space.

For comparison, we first carry out an inviscid simulation without any inertial effects due to density stratification. The density field is advected passively into Lituus spirals as is evident in figure 11. The vorticity field is not shown, but is practically unchanged from its initial configuration even at the final time. This also shows that for the

simulations considered in this paper, hyperviscous simulations suffice to reproduce inviscid behaviour.

We contrast this result with that from a full simulation including non-Boussinesq effects, shown in figure 12. It is immediately evident that density in this situation is not a 'passive' scalar, even though the Atwood number is low and there is no gravity. The vorticity profile is completely different from the simulation shown in figure 11. Vorticity of alternating sign is now produced in the form of two interwound spirals, i.e. along the density interfaces, consistent with (2.19). The vorticity across an unstable density jump is negatively signed, while positive vorticity is produced across every stable density jump. The two spiral vortex sheets we now have are unstable in the KH sense. The combined action of this and the density jumps is evident in the instability displayed at later times. The instability, once visible, grows rapidly. The spiral vortex sheet then rolls up into blobs, indicative of the dominance of the SKH instability. A final breakdown soon follows. The Atwood number in this simulation was 0.2. Note that the time $t = 30$ of the stability analysis is well before the onset of instability as can be seen in figure (12). At this time, the first visible jump in the simulations is located close to the value $1.3r_c$ used in figure 10(a). Consistent with (2.1) and the same figure, the second jump was found to occur at $1.57r_c$. The width of the vortex sheet was found to lie between $0.035r_c$ and $0.05r_c$ which is comparable to the largest value $d = 0.03r_c$ used in the stability analysis. The azimuthal wavenumber of about 11 as seen in the simulations corresponds to a wavelength of the same order of magnitude as the thickness of the interface. It compares well with a wavenumber of 8–12 obtained from the inviscid stability analysis for comparable interface thickness in figure 10(a).

A viscous simulation at $Re = 8000$ is shown in figure 13. Snapshots of the density field are also given for $Re = 6000$ and $Re = 2000$ in figure 14. The Schmidt number is fixed at 10 as in §3, and the Atwood number is 0.1. The trend in figure 13 is very similar to that in the inviscid simulation. Note that the main vortex used here is Lamb–Oseen while the stability analysis is carried out with a Rankine vortex. We therefore make only qualitative comparisons in the viscous case. A direct comparison with the viscous stability results of figure 10(b) cannot be made owing to differences in the base flow profiles. The original vortex is no longer discernible at the end of the simulation. This is in contrast to what happens when the density field is treated like a passive scalar at this Reynolds number, where the original vortex is slightly diffused but otherwise undisturbed. The inertial effects of density stratification thus act in accelerating the collapse of the vortex. Note that non-Boussinesq effects are strong even at low $\mathscr{A}$ because it is the size of the gradient of density which is important, not the density difference alone.

The instability is less clearly defined for $Re = 6000$, but one may discern that the selected wavenumber is even smaller, at about 5. No instability is visible at $Re = 2000$. A quantitative comparison of this result with the stability predictions is not straightforward due to the number of parameters involved which are sometimes difficult to estimate. The effective core becomes smaller in the simulations than the one we begin with, as discussed below, so the location of the jumps with respect to the core is difficult to estimate. The effective Atwood number in the central region decreases progressively due to the centrifugal forces making the core lighter. The thickness of the diffused layer is difficult to estimate from numerical results. Given the differences between the simulations and the idealizations made for stability analysis, both in viscous and in inviscid flow, we may conclude that a good qualitative agreement is achieved.
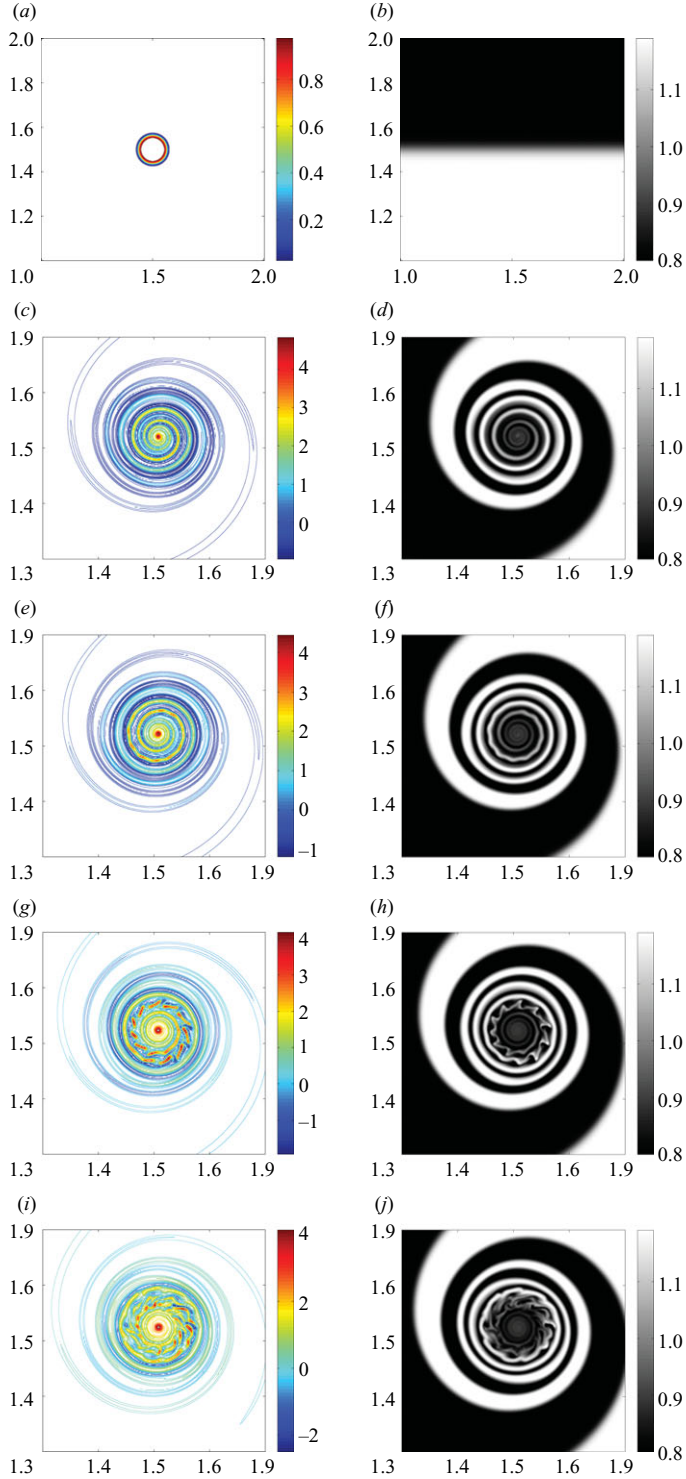
FIGURE 12. Evolution of the vorticity (*a*, *c*, *e*, *g*, *i*) and density (*b*, *d*, *f*, *h*, *j*) fields in the inviscid simulations. The time *t*, non-dimensionalized with respect to the period of rotation of the vortex core $\pi r_c^2 / \Gamma$, is 0 (*a*, *b*), 40 (*c*, *d*), 45 (*e*, *f*), 50 (*g*, *h*) and 55 (*i*, *j*). Note that the scale for (*a*, *b*) is different from others. The Atwood number is 0.2.
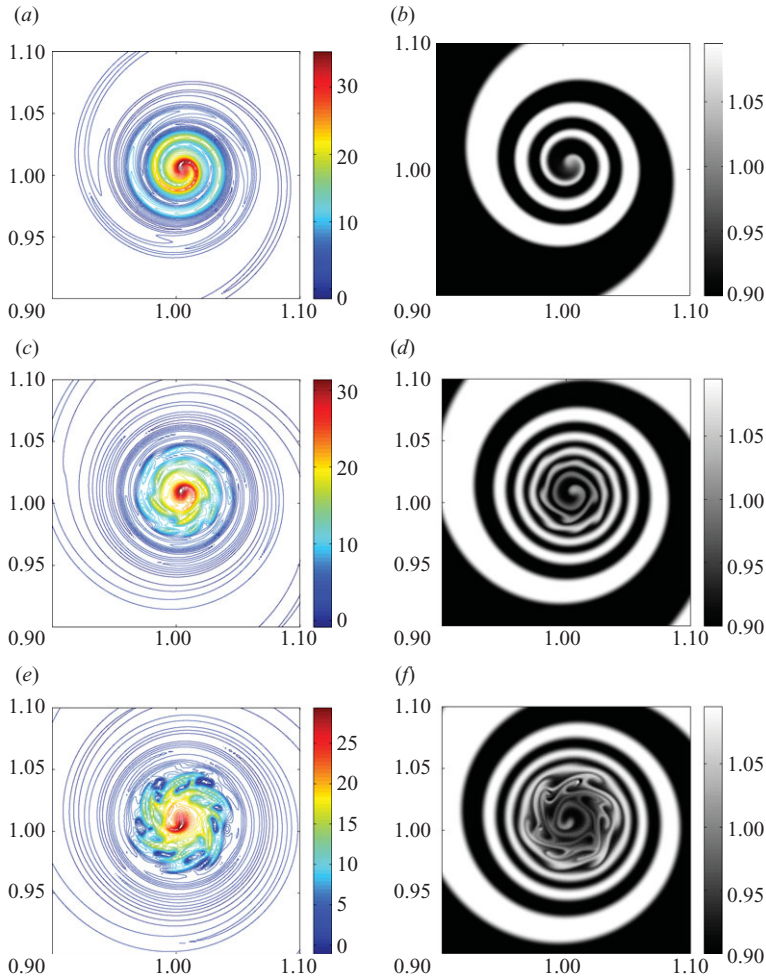
FIGURE 13. Evolution of the vorticity (*a*, *c*, *e*) and density (*b*, *d*, *f*) fields in the viscous simulations. The picture at the initial time is the same as that in figure 12, except that a Lamb–Oseen vortex is used here instead of a Rankine. The time *t*, non-dimensionalized as before, is 40.7 (*a*, *b*), 76.4 (*c*, *d*), 96.76 (*e*, *f*). The Reynolds number is 8000, the Péclet number is 80 000 and the Atwood number is 0.1.

In order to compare the growth rate with stability analysis, the amplitude of oscillation of the interface was manually extracted from the numerical data. This was possible to do relatively reliably only for the inviscid simulations, and so we present results for only this case. The instability becomes visible after a time $t > 44$. The amplitude η of a given undulation was measured by hand at various times, after $t = 44$ when the instability becomes visible, till nonlinear effects become important at $t \sim 53$. The superimposition of two such measurements at different phases is shown in figure 15. A exponential fit gives growth as $\exp(0.32t)$. At the time and innermost radius of onset of instability, it was estimated that the thickness of the spiral interface was approximately $0.05r_c$. In the instability predictions of figure 10(*a*), ω_i for this case is approximately 0.37. The jump in velocity in the stability analysis was prescribed to match the simulations, but there are still many differences between direct simulations
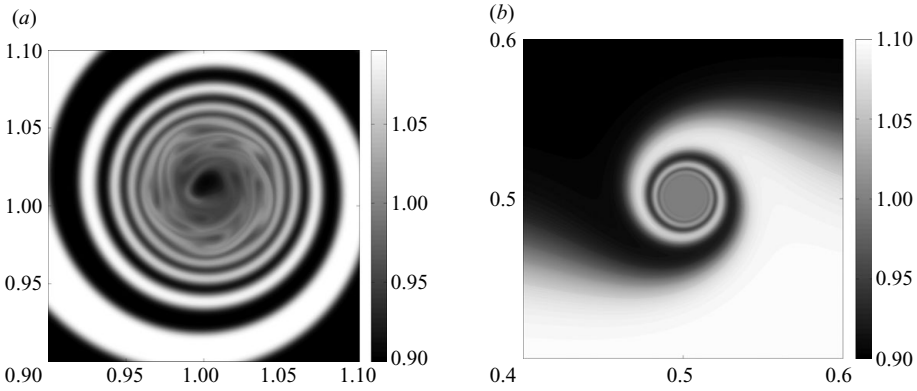
FIGURE 14. Snapshot of the density field in a viscous simulations with (*a*) $Re = 6000$, $Pe = 60\,000$ and (*b*) $Re = 2000$, $Pe = 20\,000$. The instability in (*a*) is qualitatively similar to figure 13, whereas there is no instability in (*b*) owing to smaller centrifugal forces and more rapid homogenization.
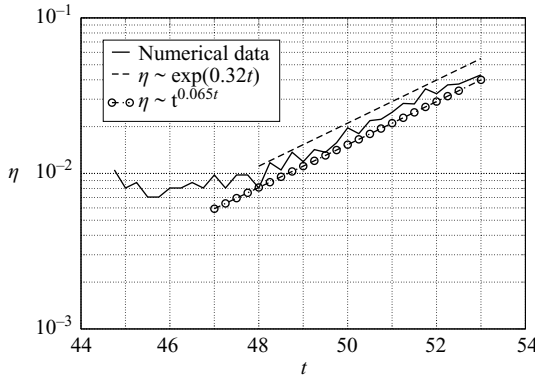

FIGURE 15. Growth rate extracted from the numerical simulation of figure 12. The straight line is an exponential fit. The stability analysis of figure 10(*a*) predicted a growth as $\exp(0.37t)$.

and the stability analysis of a simplified problem. This comparison may thus be considered quite good. In §1 the SKH disturbance amplitude was predicted to grow as t^{bt}. Given the small duration of the numerical instability is is difficult to differentiate between this and a pure exponential growth. A fit of this form is also shown in figure 15, with $b \sim \omega_i / t_{avg}$ where $t_{avg} \approx 50$.

In the simulations, since we have a density interface of finite thickness, two points on the interface initially separated by a small distance l_0 are stretched apart due to the spiralling. We have from (2.15),

$$\frac{l(r,t)}{l_0} = \theta_s. \tag{4.4}$$

Due to this steepening of the density gradient, Gibbs oscillations were encountered at the later stages of these simulations which prevented the study of the complete breakdown of the vortex cores. Secondly, in the viscous simulations, at the Reynolds numbers considered, the grid is not sufficient to resolve all the scales up to the Kolmogorov scale. Hence, a correct fully turbulent state cannot be achieved in these
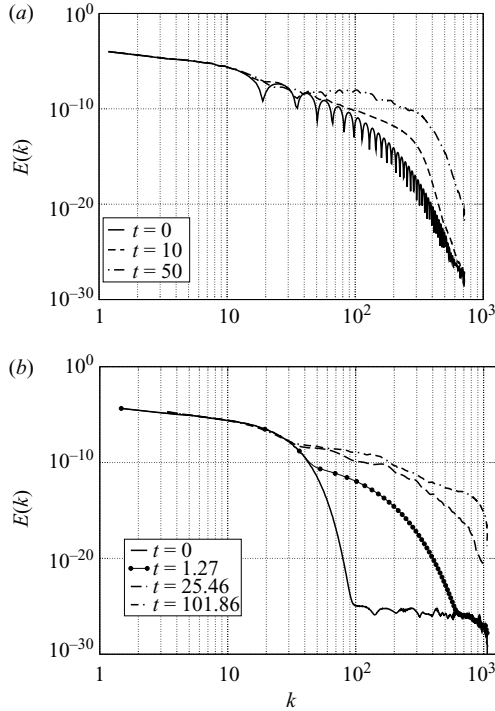
FIGURE 16. The energy spectrum for the (*a*) inviscid and (*b*) viscous simulations at $Re = 8000$.

simulations. Nevertheless, an examination of the energy spectrum is a useful indicator of the cascade effects. Figures 16(*a*) and 16(*b*) show the kinetic energy spectrum for the inviscid and the viscous simulations respectively, plotted against the scale $k = (k_x^2 + k_y^2)^{1/2}$. The difference between the inviscid and viscous spectra at the initial time is because in the latter we use a Lamb–Oseen vortex, while in the former, a Rankine vortex is used, which includes sharp changes in the velocity derivative at the edge of the vortex core. This produces a signal with sharp dips at the zeros of the Bessel function J_1 (Neilsen *et al.* 1996). This is because the energy spectrum for an axisymmetric vortex is given by $E(k) = \pi/k \int \Omega(r) J_0(kr) dr$ (Gilbert 1988), so for a Rankine vortex we get $E(k) \propto J_1(kr)$, and a steep tanh vorticity profile behaves similarly.

As time progresses, both spectra broaden and flatten, corresponding to the emergence of smaller scales. The final state is turbulence-like, but the simulations are insufficient to make more quantitative statements. In the case of gravity driven flows, an exchange takes place between the kinetic and potential energies, often with one growing at the expense of the other. It is instructive to construct an analogy to this process in the present system. The total energy, given by $E_t = \int \int \tilde{\rho}/2(u^2 + v^2) dV$, is a conserved quantity in the absence of viscosity. Writing $\tilde{\rho} = \rho_{ave} + \hat{\rho}$ where ρ_{ave} is constant, we have

$$E_t = E + E_\rho, \tag{4.5}$$

where $E \equiv \rho_0 \int_0^L \int_0^L (u^2 + v^2)/2 \, dxdy$ is the kinetic energy based on a constant density, i.e. the integrand is just the kinetic energy per unit mass, a useful quantity in stratified flows (Gill 1982). The second term $E_\rho \equiv \int \int \hat{\rho}/2(u^2 + v^2) dV$ is analogous to a potential energy in a system with radial (centrifugal) gravity ($\sim \Gamma^2/r^3$), and arises solely due to inhomogeneity in the density field. Such a splitting of the total energy
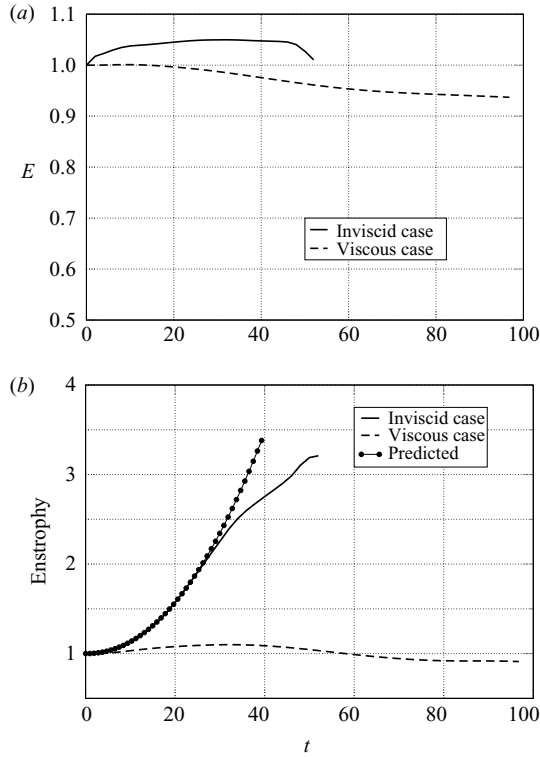
FIGURE 17. (*a*) Variation of E (kinetic energy based on a constant density) with time for the inviscid and viscous simulations. (*b*) Variation of total enstrophy with time. Solid line: inviscid simulations; dashed line: viscous simulations at $Re = 8000$. Symbols: predictions based on §2.2.

E_t highlights the contribution of the density variations, since the quantity E increases or decreases at the expense of E_ρ. Figures 17(*a*) and 17(*b*) show the evolution of E and enstrophy ($Z = \int_0^L \int_0^L \Omega^2 \mathrm{d}x\mathrm{d}y$) with time, normalized by their initial value. The residual vorticity is first subtracted from the total vorticity field, from which the velocity field is calculated. Both the energy and the enstrophy here are calculated in the physical space. The slight increase in E visible in the inviscid case is due to density variations acting as a source. In the viscous case this increase is offset by the dissipation. The net enstrophy in the inviscid case increases continuously since vorticity is generated continuously at the density interface. The viscous case shows a small increase at short times and a decay at long times. The difference in enstrophy production could arise from increased diffusion of the interface, and from the different initial vorticity distribution. From Kelvin's law, for a given strength ΔU_θ of the vortex sheet, the vorticity created in the spiral (defined in (2.21)) would increase due to the stretching of the density interface by the factor given in (4.4). With this taken into account, the prediction of the total enstrophy is seen in figure 17(*b*) to agree well with the inviscid simulations up to some time. The prediction, being for a point vortex, is of arbitrarily scale so the scales are chosen to match the simulations.

The reduction in instability at large r is easily expected from our analysis, but it remains to be explained why the instability first begins at a specific radial location, as observed in figures 12 and 13. From (2.3) the homogenized region around a
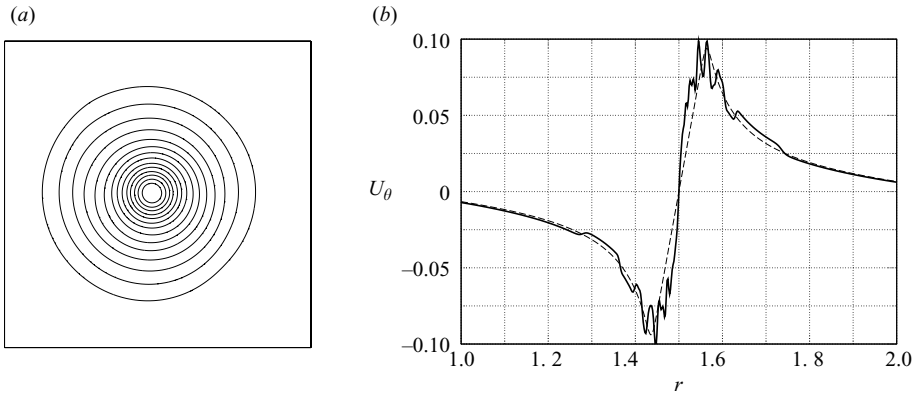
(a)

(b)

FIGURE 18. (a) Nearly axisymmetric streamlines near the onset of instability for a Rankine vortex. The time is 50, and the corresponding vorticity and density profiles are shown in figures 12(g) and 12(h) respectively. (b) Azimuthal velocity for a Rankine vortex at the initial time (symbols) and at t = 50 (solid line).

point vortex scales as $r_h \sim \kappa^{1/6}$ for a diffusive flow. In the hyperdiffusive case, similar arguments lead us to $r_h \sim \kappa_h^{1/18}$. The prefactor in these scalings is difficult to estimate, but we may appreciate that the homogenization in the two simulations is comparable, and not too small by the time the instability becomes visible. The instability thus appears just outside r_h, at the first surviving jump. In §2.2, we assumed that the dominant effect on the base flow was from a central vortex, and that the streamlines would remain circular. The assumption is validated by the streamlines of the inviscid simulations plotted in figure 18(a). The radial variation of azimuthal velocity at $t = 50$, seen in figure 18(b), is also consistent with predictions. It is also noticed that the central vortex becomes significantly smaller and stronger at early times, while more or less maintaining its circulation constant. The reason for this is that the simulations begin with a straight density interface within the vortex core, which is rotated around at early times like a solid object. This results in the production of opposite-signed vorticity on two halves of the interface within the core, so one part of the core becomes stronger and the other weaker. The weaker part is then entrained by the stronger part to give a smaller and stronger core slightly shifted away from the original centre. A similar drift due to an asymmetric vorticity distribution was seen by Bajer, Bassom & Gilbert (2004).

5. Discussion

It emerges from this study that the neglect of inertial effects of density stratification is often not valid in the vicinity of a vortex in density-stratified flows. This is the case even when the difference of density is small, so long as the interface is thin, making the density gradient significant, and even when gravity is absent. Non-Boussinesq effects are especially large in high-Péclet-number flows, and where density changes over a thin layer. This has been demonstrated by following the evolution of a system consisting of a lone vortex at an initially flat density interface. The evolution of this system into a spiral density interface at first, followed by vorticity generation everywhere on the spiral interface, giving rise to instability and breakdown is predicted by stability theory and shown to be in qualitative agreement with direct numerical simulations, both inviscid and viscous. The density field, which would merely have advected as a

passive scalar if non-Boussinesq effects were neglected, now causes an instability of a combined centrifugal RT and spiral KH type. The centrifugal term takes the place of gravity to cause the RT instability. Unlike earlier work on CRT instability, the present flow is unstable in the RT sense whether the innermost region is light or heavy. This is because the tightly wound spirals give rise to density jumps of alternating sign. The small deviation of the spiral from a perfectly circular shape means that the density gradient is not perfectly perpendicular to the centripetal acceleration. The result is two oppositely signed spiral vortex sheets whose strength increases logarithmically in time. The spiral KH instability which ensues therefore grows as t^t. Both instabilities give rise to large growth rates, with the SKH dominating at large times. Note that this prediction is made here by an idealized inviscid model. Physically, the continuous generation of fresh vorticity at the density interfaces stoking the already unstable exponential instability, leads one to expect a super-exponential behaviour. However the difference between the form t^t and that of a pure exponential growth is small, and the present simulations are not able to distinguish between them. A larger computation where the interface could be resolved better everywhere, and the growth rate could be gleaned to better accuracy, would be needed to check this prediction. At small interface thickness, the dominant m in inviscid SKH+CRT instability is dictated by the interface thickness. For higher interface thickness a flapping mode is observed, with significantly lower m. The viscous analysis shows that decreasing the Reynolds number, decreasing the Atwood number and increasing the interface thickness all have a stabilizing effect, as is to be expected. Decreasing the Reynolds number results in a reduction of the dominant wavenumber as well. A detailed parametric study for the viscous case is warranted.

The azimuthal wavenumbers seen in the viscous and inviscid simulations were in good qualitative agreement with the stability results. For $\mathscr{A} = 0.1$, no instability was noticed for $Re \leqslant 2000$, while the critical Reynolds number for this Atwood number and comparable thickness was slightly lower in the stability studies. The grid used in the present simulations is insufficient to completely resolve the final turbulence-like state, but the breakdown into a spectrum of small scales, and the annihilation of the original vortex are evident.

Since inertia and the effective gravity are dictated by the same scales in this flow, the effective Froude number based on $\Delta\rho$ is of $O(\mathscr{A}^{-1/2})$. For a thin density interface, the effective Froude number, which depends on the density gradient rather than on the density difference, would be much lower $\sim (\mathscr{A}\rho'r/\rho)^{-1/2}$, so density would play a lead role for thin interfaces.

The effect of continuous density stratification is being studied, especially in the context of vortex merger. The effect of three-dimensionality and the competition between the new instabilities which would then occur is also of interest.

REFERENCES

BAJER, K., BASSOM, A. P. & GILBERT, A. D. 2001 Accelerated diffusion in the centre of a vortex. *J. Fluid Mech.* **437**, 395–411.

BAJER, K., BASSOM, A. P. & GILBERT, A. D. 2004 Vortex motion in a weak background shear flow. *J. Fluid Mech.* **509**, 281–304.

BILLANT, P. & CHOMAZ, J.-M. 2000 Experimental evidence for a new instability of a vertical columnar vortex pair in a strongly stratified fluid. *J. Fluid Mech.* **418**, 167–188.

BRANDT, L. K. & NOMURA, K. K. 2007 The physics of vortex merger and the effects of ambient stable stratification. *J. Fluid Mech.* **592**, 413–446.

CHANDRASEKHAR, S. 1961 *Hydrodynamic and Hydromagnetic Stability*. Clarendon Press.

COQUART, L., SIPP, D. & JACQUIN, L. 2005 Mixing induced by Rayleigh–Taylor instability in a vortex. *Phys. Fluids* **17**, 021703.

CROW, S. C. 1970 Stability theory for a pair of trailing vortices. *AIAA J.* **8**, 2172–2179.

DRAZIN, P. G. & REID, W. H. 1981 *Hydrodynamic Stability*. Cambridge University Press.

DUFF, R. E., HARLOW, F. H. & HIRT, C. W. 1962 Effects of diffusion on interface instability between gases. *Phys. Fluids* **5**, 417–425.

FLOHR, P. & VASSILICOS, J. C. 1997 Accelerated scalar dissipation in a vortex. *J. Fluid Mech.* **348**, 295–317.

FONTANE, J. & JOLY, L. 2008 The stability of the variable-density Kelvin–Helmholtz billow. *J. Fluid Mech.* **612**, 237–260.

FUNG, Y. T. 1983 Non-axisymmetric instability of a rotating layer of fluid. *J. Fluid Mech.* **127**, 83–90.

FUNG, Y. T. & KURZWEG, U. H. 1975 Stability of swirling flows with radius-dependent density. *J. Fluid Mech.* **72**, 243–255.

GILBERT, A. D. 1988 Spiral structures and spectra in two-dimensional turbulence. *J. Fluid Mech.* **193**, 475–497.

GILL, A. E. 1982 *Atmosphere–Ocean Dynamics*. Academic Press.

GREENSPAN, H. P. 1968 *The Theory of Rotating Fluids*. Cambridge University Press.

HOWARD, L. N. & GUPTA, A. S. 1962 On the hydrodynamic and hydromagnetic stability of swirling flows. *J. Fluid Mech.* **14**, 463–476.

ITANO, T. 2004 Stability of an elliptic flow with a horizontal axis under stable stratification. *Phys. Fluids* **16**, 1164–1167.

JOLY, L., FONTANE, J. & CHASSAING, P. 2005 The Rayleigh–Taylor instability of two-dimensional high-density vortices. *J. Fluid Mech.* **537**, 415–431.

JOSSERAND, CH. & ROSSI, M. 2007 The merging of two co-rotating vortices: a numerical study. *Eur. J. Mech.* B/*Fluids* **26**, 779–794.

KERSWELL, R. R. 2002 Elliptical instability. *Annu. Rev. Fluid Mech.* **34**, 83–113.

KHORRAMI, M. R., MALIK, M. R. & ASH, R. L. 1989 Application of spectral collocation techniques to the stability of swirling flows. *J. Comput. Phys.* **81**, 206–229.

LEIBOVICH, S. 1969 Stability of density stratified rotating flows. *AIAA J.* **7**, 177–178.

LIN, C. C. 1955 *The Theory of Hydrodynamic Stability*. Cambridge University Press.

MIYAZAKI, T. & FUKUMOTO, Y. 1992 Three dimensional instability of strained vortices in a stably stratified fluid. *Phys. Fluids* A **4**, 2515–2522.

MOFFATT, H. K. & KAMKAR, H. 1983 The time-scale associated with flux expulsion. In *Stellar and Planetary Magnetism* (ed. A. M. Soward), pp. 91–97. Gordon and Breach.

NEILSEN, A. H., HE, X., RASMUSSEN, J. J. & BOHR, T. 1996 Vortex merging and spectral cascade in two-dimensional flows. *Phys. Fluids* **8**, 2263–2265.

REINAUD, J., JOLY, L. & CHASSAING, P. 2000 The baroclinic secondary instability of the two-dimensional shear layer. *Phys. Fluids* **12**, 2489–2505.

RHINES, P. B. & YOUNG, W. R. 1983 How rapidly is a passive scalar mixed within closed streamlines? *J. Fluid Mech.* **133**, 133–145.

SAUNDERS, P. M. 1973 The instability of a baroclinic vortex. *J. Phys. Oceanogr.* **3**, 61–65.

SIPP, D., FABRE, D., MICHELIN, S. & JACQUIN, L. 2005 Stability of a vortex with a heavy core. *J. Fluid Mech.* **526**, 67–76.

VILLERMAUX, E. 1998 On the role of viscosity in shear instabilities. *Phys. Fluids* **10**, 368–373.

YIH, C. S. 1961 Dual role of viscosity in the instability of revolving fluids of variable density. *Phys. Fluids* **4**, 806–811.